John-Alexander Preuss [ID]
Gia Nam Nguyen
Virginia Berk
Janina Bahnemann [ID]

Institute of Technical Chemistry,
Leibniz University Hannover,
Callinstraße 5, Hannover, 30167,
Germany

Research Article

Miniaturized free-flow electrophoresis: production, optimization, and application using 3D printing technology

The increasing resolution of three-dimensional (3D) printing offers simplified access to, and development of, microfluidic devices with complex 3D structures. Therefore, this technology is increasingly used for rapid prototyping in laboratories and industry. Microfluidic free flow electrophoresis (μFFE) is a versatile tool to separate and concentrate different samples (such as DNA, proteins, and cells) to different outlets in a time range measured in mere tens of seconds and offers great potential for use in downstream processing, for example. However, the production of μFFE devices is usually rather elaborate. Many designs are based on chemical pretreatment or manual alignment for the setup. Especially for the separation chamber of a μFFE device, this is a crucial step which should be automatized. We have developed a smart 3D design of a μFFE to pave the way for a simpler production. This study presents (1) a robust and reproducible way to build up critical parts of a μFFE device based on high-resolution MultiJet 3D printing; (2) a simplified insertion of commercial polycarbonate membranes to segregate separation and electrode chambers; and (3) integrated, 3D-printed wells that enable a defined sample fractionation (chip-to-world interface). In proof of concept experiments both a mixture of fluorescence dyes and a mixture of amino acids were successfully separated in our 3D-printed μFFE device.

Additional supporting information may be found online in the Supporting Information section at the end of the article.

1 Introduction

In recent years, three-dimensional (3D) printing has been the focus of increasing attention in the community of microfluidics. 3D printing refers to various additive manufacturing techniques, of which many belong to the group of rapid prototyping tools. One of the biggest advantages of 3D printing includes the direct buildup of a desired model from a computer-aided design (CAD) file without the need for any master mold or clean room facilities [1,2]. Moreover, complex 3D structures—as they are used for example in passive micromixers—do not need any potentially error-prone annealing steps, and manual labor is considerably reduced when compared to more traditional assembly methods [3–5]. Manufacturing of polydimethylsiloxane-based (PDMS) devices typically requires a master mold for each design, as well as assembly of each casting [6–8]. In addition to the casting methods, subtractive methods are used to fabricate microfluidic devices [9,10]. For example, it has been shown that microstructures for a capillary electrophoresis device in poly(methyl methacrylate) (PMMA) can be produced by laser engraving within seconds [9]. However, a major disadvantage of this method is that structures can usually only be lasered into the material in 2Ds. More complex microsystems with internal 3D structures cannot be manufactured in one piece and therefore an assembly would be necessary.

Although the printing resolution often does not yet meet the performance standards set by standard techniques, channels in the range of 80 μm in height have been shown to be manufacturable for microfluidic applications by 3D printing [11,12].

Correspondence: Dr. Janina Bahnemann, Institute of Technical Chemistry, Leibniz University Hanover, Callinstr. 5, 30167 Hannover, Germany
E-mail: jbahnemann@iftc.uni-hannover.de

Abbreviations: 3D, three-dimensional; **CAD**, computer-aided design; **FDM**, fused deposition modeling; **HEC**, 2-hydroxyethyl cellulose; **μFFE**, microfluidic free-flow electrophoresis; **PTFE**, polytetrafluoroethylene

Color online: See article online to view Fig. 1 in color.

MultiJet Printing—as employed in this publication—is a 3D printing technique which is comparable to common inkjet printing, where a finite number of 2D layers build up the device. To enable complex overhanging structures, a wax support material is applied alongside a photocurable resin which serves as the primary material. The wax can be removed by melting and flushing at ambient temperatures [3,4]. Recently, our group has shown the biocompatibility of the acrylic material following different sterilization procedures for mesenchymal stem cells—a crucial prerequisite if 3D printing is to serve as a serious alternative to lab-on-a-chip (LoC) devices made from PDMS, poly(methyl methacrylate) (PMMA), or glass [13,14].

Microfluidic free-flow electrophoresis (µFFE) is an example of a LoC device which can separate complex samples (e.g., nucleic acids [15–17], proteins [6,7,11,18–21], and cells [22,23]) in a continuous manner. Usually, the electric field is applied perpendicularly to the fluidic stream, and charged compounds are deflected differently based on their specific electrophoretic mobility [24,25]. Although µFFE benefits from comparatively fast separation, low volumes, and high voltage efficiencies compared to its macrofluidic counterpart, the microfluidic application does suffer from electrolysis-based bubble formation as a source of error [25]. Consequently, research in this field has increasingly focused on the prevention of fluidic and electrical inhomogeneity due to bubble formation. To prevent bubbles from entering the main chamber, strategies such as deepening electrode channels for an highly increased volume flow rate [11,12,26], (high resistance) side channels [27,28] between separation channel and electrode channel, and gels [22,23,29,30] and membranes [7,17,31] have been developed. Further techniques include mediation of the electric field through an insulating barrier [32], and chemical suppression of electrolysis [33]. Herzog et al. were the first to establish gas removal through a nanoporous polytetrafluoroethylene (PTFE) membrane—thus enabling a long-term run with a high electric field of 500 V/m [34]. However, that setup consists of five layers that must all be carefully aligned.

Barrier-free, fluidic solutions require precise flow control and have been used in the (to date) only two µFFE designs that are based on 3D printing [11,12,26,35]. Moreover, all published 3D-printed µFFE devices depend on an assembly of a top and a bottom part. A change of design with regard to channel dimensions or number of outlets might require further adjustments, however. Focusing on mechanical segregation, the ideal barrier promises low electrical resistance while acting as a hydrodynamic barrier for bubble entries (and even for high flow rates) in the electrode chambers which do not impact the fluidics of the separation chamber [7]. First presented by Novo et al. [7,17], commercially available polycarbonate membranes meet these criteria and allow simple integration into the PDMS-based device. In this study, a novel 3D design of a microfluidic device is presented, which allows an easy, fast, and cost-effective production of a µFFE using high-resolution 3D printing technology. Notably, the 3D printing process does not require any clean room facilities and can be

accomplished within a few hours from design to separation experiments. Moreover, the design can be quickly adapted if necessary and essential functional parts (such as connectors, interfaces, or sample fractionation) can be directly integrated into the desired system. As a proof of concept, three different fluorophores and three different rhodamine B labeled amino acids were separated by a zone electrophoresis mode in the 3D-printed µFFE and fractionated into integrated 3D-printed wells (chip-to-world interface).

2 Materials and methods

2.1 Chemicals

3D printing material M2R-CL and support material M2-SUP was purchased from 3D Systems (Rock Hill, USA). For post-processing, paraffin oil (Carl Roth GmbH, Karlsruhe, Germany) and regular dishwashing detergent (Fairy Ultra Plus, Procter and Gamble, Cincinnati, USA) were used. The super glue was purchased from Stylex Schreibwaren GmbH (Bad Bentheim, Germany).

The separation buffer was prepared using 10 mM HEPES (VWR International GmbH, Darmstadt, Germany), 20 mM Bis-tris (AppliChem GmbH, Darmstadt, Germany), 0.1% w/v 2-hydroxyethyl cellulose (HEC, molecular weight of 1300000; Merck KGaA, Darmstadt, Germany), at pH 8. HEC is a neutral cellulose derivative which is used as buffer derivative to suppress electroosmotic flows by dynamic coating. [7,36] The labeling buffer consisted of 50 mM sodium carbonate buffer (Merck), pH 10. All buffers were prepared in 18.2 MΩ•cm water. The fluorescence dyes sulforhodamine B (technical grade), pyronin Y (for nucleic acid electrophoresis), and rhodamine B were purchased from Merck. All fluorescence dyes were solved in separation buffer to a final concentration of 200 µM. For the determination of EOF, rhodamine B was used as the only dye in the sample stream.

Rhodamine B isothiocyanate was purchased from Santa Cruz Biotechnology, Inc. (Heidelberg, Germany). Glycine, arginine, and sodium glutamate were obtained from Merck (purity > 99%).

2.2 Design and fabrication

As a first step in the manufacturing process, a 3D computer-aided design model (CAD) was constructed. The 3D CAD software SolidWorks 2018 (Dassault Systèmes SolidWorks Corp, Waltham, MA, USA) was used for the design of all 3D-printed devices. The designed CAD model was saved as an .STL file and was sent directly to the 3D printer (MJP 2500 Plus MultiJet printer, 3D Systems, Rock Hill, USA), which produced the model. The corresponding .STL files are provided in the Supporting Information. After the printing process, the 3D-printed parts remain on the printing platform. An efficient way to gently remove the parts from the printing platform is to cool the 3D-printed devices at −18°C for
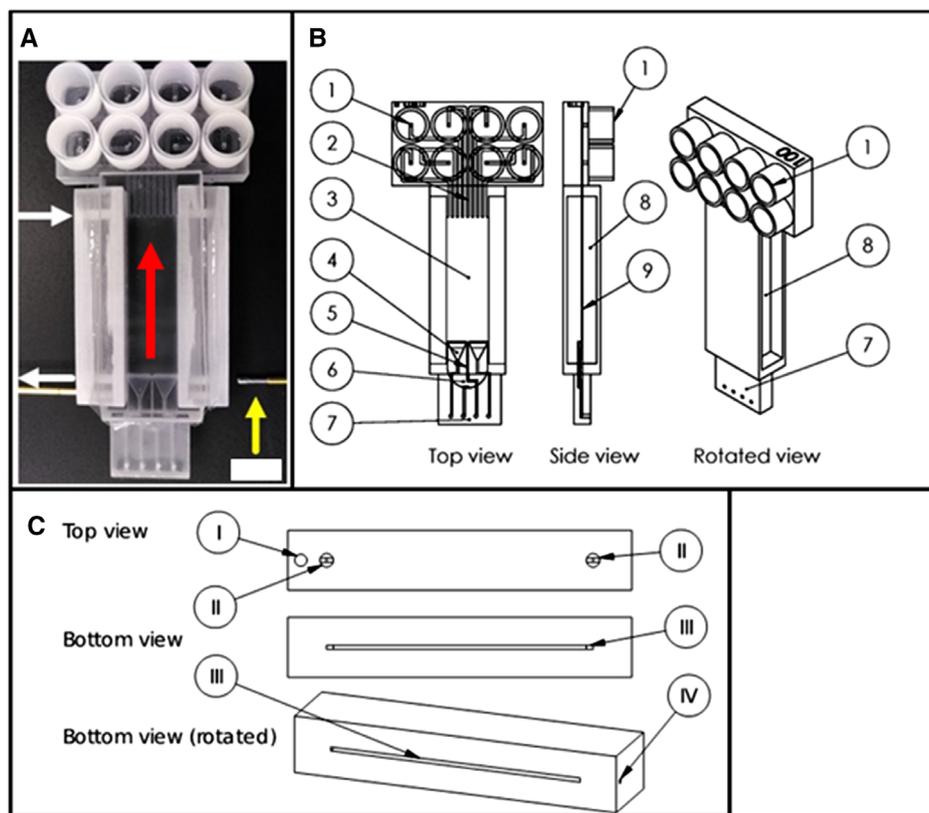
Figure 1. (A) 3D-printed μFFE device. The red arrow indicates the flow direction from the main chamber's inlets towards the outlet channels. The white arrows indicate the flow through the electrode chamber. The yellow arrow points towards one of the contact tips. The white scale bar represents 10 mm of width. (B) Different views of the CAD for the main part (1: 3D-printed wells; 2: Outlet channels; 3: Separation chamber; 4: Buffer inlet; 5: Sample inlet; 6: Inlet for the flushing solution; 7: Adapter for the microfluidic connector; 8: Cavity for the side part/electrode chamber; 9: 100 μm slit towards the separation chamber). (C) Different views of the CAD for the side part/electrode chamber (I: Hole for the contact tip; II: Inlet and outlet for tubing; III: Electrode chamber; IV: Inlet for the platinum wire).

10 min [37]. Afterwards, the wax support material was removed with a 3D Systems EasyClean unit, which consists of a water vapor bath and a paraffin oil bath (3D systems, Rock Hill, USA). Oil residues were then removed in an ultrasonic bath (Elma Elmasonic S30 H, Elma, Schmidbauer GmbH, Singen, Germany) with warm soapy water (50°C) run at least three times—and the device was subsequently further cleaned with distilled water. Interior structures were cleaned simultaneously by flushing with a syringe under the same conditions. The platinum wires were placed into their corresponding holes in the electrode chambers (see Fig. 1C). The polycarbonate membrane (pore size of 0.1 μm; Whatman Nuclepore Track-Etched Membrane, Merck) was cut into 40 mm × 7 mm rectangles, and placed into the cavity of the main chamber of the 3D-printed μFFE. The side parts were pressed onto the polycarbonate membranes, and the device's edges were then sealed by gluing using super glue for at least 30 min. Contact tips were pressed onto the platinum wires through the corresponding holes. For continuous purging of the side parts during the electrophoretic experiments, two PTFE tubes (Bohlender GmbH, Grünsfeld, Germany) were stuck into the corresponding holes of each side part.

2.3 Measuring the accuracy of 3D printing

To investigate the accuracy of the channel heights of the outlet channels and the main chamber microscopically, the μFFE

devices were designed and 3D-printed as open models without the upper channel ceiling. The profiles of the 3D-printed models were recorded by stepwise automatic change of the *z*-position of the focal plane (VHX-6000 digital microscope, KEYENCE Deutschland GmbH, Neu-Isenburg, Germany). The profile of a feature can be determined by matching sharp pixels and the *z*-position of the image. Two different channel heights were designed and examined—one at 100 μm, and another at 200 μm. In total, three technical replicates were measured at three different positions (see Fig. 2 for further information).

In particular, the 3D panorama function of the digital microscope was applied to record the outlet channels (200x magnification). The total difference of Z boundaries was set to 500 μm. The line for the profile was set over the entire width of the channel (perpendicular to the channels). The channel height was determined as the difference between the wall height and the bottom of a channel (please note that each channel has two walls, resulting in two depths per channel). The surface roughness parameter "R_a" (an arithmetical mean deviation of the assessed profile) was determined by the function line roughness of the microscope.

2.4 Determination of outlet precision

The total flow rate of the main chamber of the μFFE was set to 100 μL/min for 13 min (main chamber height of 100 μm).
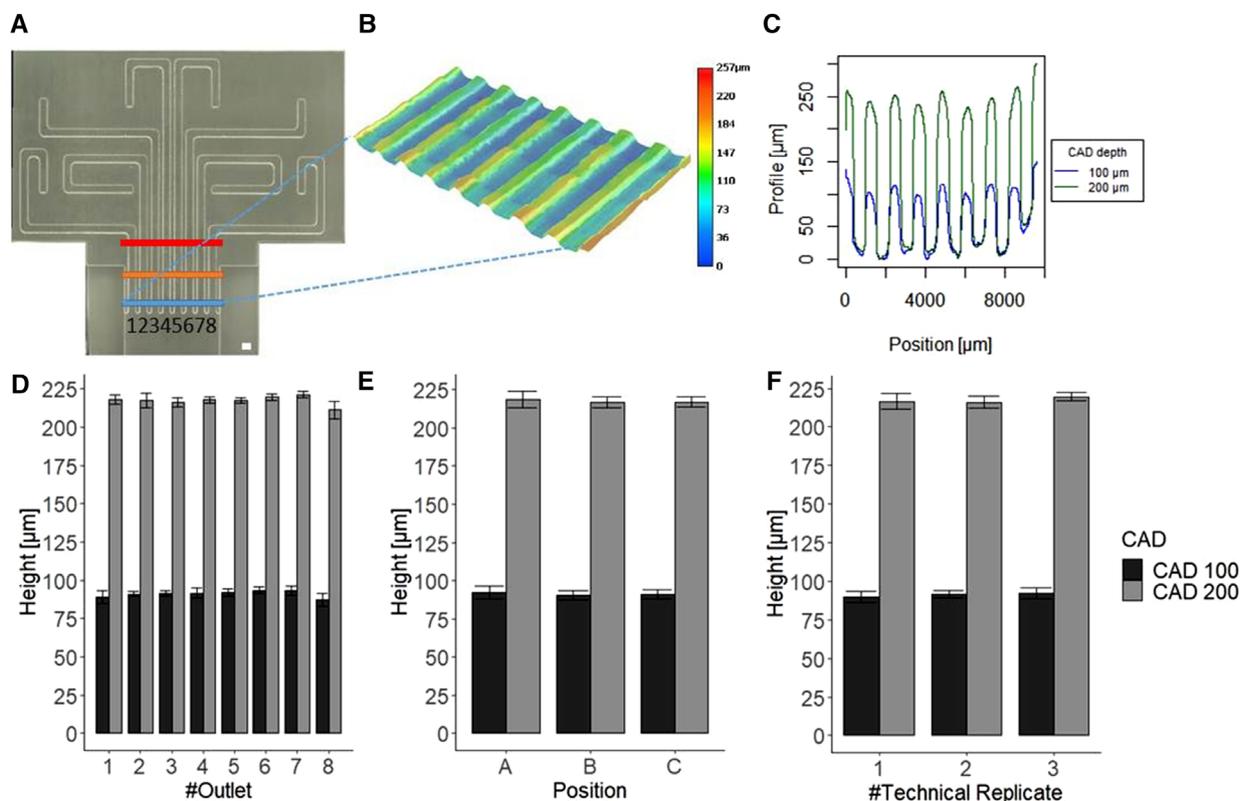
Figure 2. (A) Image of 3D-printed channels (CAD height of 100 μm). The numbers indicate the outlet number. White scale bar displays a width of 1 mm. The blue, orange, and red lines indicate the positions A, B, C for the profile measurements. (B) 3D-microscopic image of the 3D-printed channels (CAD depth of 100 μm). (C) Depth profiles of 3D-printed outlet channels (numbering corresponds to the outlet numbering). (D) Mean channel height of outlet channels (error bars display the standard deviation for three technical replicates and three positions). (E) Mean channel height of different positions (error bars display the standard deviation for three technical replicates and eight different channels). (F) Mean channel height of technical replicates (error bars display the standard deviation for three different positions and eight channels.)

The flow rate corresponds to the flow rate of separation experiments. Each side part was flowed with a flow rate of 200 μL/min while a medium voltage of 90 V was applied. The outlet precision was determined gravimetrically. In particular, the volume collected in each 3D-printed well was transferred to a reaction tube. The net weight of the volume was compared to the total net weight of the volume within all 3D-printed wells of a single run. The outlet precision was measured for each technical replicate ($n = 3$) in triplicate.

2.5 Labeling of amino acids

Stock solutions of 10 mM glycine, 10 mM sodium glutamate, and 10 mM arginine, were each solved in labeling buffer (50 mM carbonate buffer, pH 10). 50 μL of a fresh 2 mg/mL solution of rhodamine B isothiocyanate in dimethyl sulfoxide (DMSO) were added to 1 mL of each amino acid solution. The reaction was kept in the dark for two days and shaken at room temperature at 700 rpm using a Thermomixer compact from Eppendorf AG (Hamburg, Germany). Labeled amino acids were stored in the dark at +4°C. For electrophoretic experiments, 266 μL each of the labeled amino acid solutions

were mixed with 200 μL 5x separation buffer (50 mM HEPES, 100 mM Bis-Tris, and 0.5% HEC, pH 8).

2.6 Setup of electrokinetic experiments

In general, the 3D-printed microfluidic devices were connected to PTFE tubing (Bohlender GmbH, Grünsfeld, Germany) by a 4-way linear connector and top interface (The Dolomite Centre Ltd, Royston, UK), and were connected via Luer lock (IDEX Health & Science LLC, Oak Harbor, USA) to 1 mL or 10 mL syringes. The volume flow rates were set by programmable syringe pumps (Aladdin AL1000-220, World Precision Instruments GmbH, Friedberg, Germany) and are specified in each materials and methods section. The fully assembled device was placed onto an inverted fluorescence microscope (Olympus IX50, Olympus Deutschland GmbH, Hamburg, Germany) and the contact tips were connected to a PLH120 power supply (Aim-TTi International, Huntingdon, United Kingdom) by a KLEPS 2600 RT Security Clamping Test Tip (4 mm) (SKS-Kontakttechnik GmbH, Niederdorf, Germany). Pictures and videos were taken by Microscope Camera HPU 10MP (Windaus-Labortechnik GmbH & Co.

KG, Clausthal-Zellerfeld, Germany). If necessary, the flushing tube was used to purge any remaining bubbles from the chamber after initial filling.

Electrophoretic experiments were carried out at different voltages from 0 V up to 120 V. The chamber height of the µFFE was 100 µm. The total flow rate of the separation buffer was set to 100 µL/min for the separation of fluorescence dyes. The sample stream, a mixture of 200 µm pyronin Y, 200 µm sulforhodamine B, 200 µm rhodamine B, had a flow rate of 1 µL/min. In a further experiment, the sample stream contained rhodamine B labeled amino acids (180 µm glycine, 180 µm glutamate, and 180 µm arginine), while the total flow rate of the separation buffers and the sample stream was set to 200 µL/min and 2 µL/min, respectively.

To estimate the impact of EOF, 200 µm rhodamine B was used as the only fluorescence dye. Compared to dyes with a positive or negative charge, band broadening of electrically neutral rhodamine B occurs only by EOF and has no electrophoretic origin. Moreover, band broadening increases with channel height (for further details see Section 3.4, Eq. (1)) [38]. Usually, the channel height is reduced for electrophoretic experiments in order to minimize band broadening. However, an increased band broadening due to an increased channel height offers a more precise measurement of the electroosmotic mobility as key parameter to describe the impact of EOF. Since the value of the electroosmotic mobility is independent on the geometry, it can be used to compare different materials with regard to their impact on EOF. In this experiment, the band width of rhodamine B inside the main channel (increased CAD height of 200 µm) was measured at a voltage of 0 V and 120 V. The flow rates were the same as for the separation of rhodamine B, sulforhodamine B, and pyronin Y. The apparent electroosmotic mobility was determined for each technical replicate ($n = 3$) in triplicate. ImageJ was used for image analysis (Fiji [39,40]).

3 Results and discussion

3.1 Design and fabrication

3D printing is an emerging tool for small-scale manufacture of microfluidic applications in general [4]. To be a true alternative for existing manufacturing processes, 3D printing must offer paths for a simplified setup. With regard to µFFE as a method for continuous electrophoretic separation, we focused on three principles for a simplified setup. First, 3D printing offers an opportunity for a higher degree of automation and rapid prototyping. Second, alignment should be avoided whenever possible. Especially, to build up bottom and top of the separation chamber in a single step is key. Third, the strategy chosen to prevent bubbles from entering the main chamber should not result in a complicated adjustment of flow rates. In Fig. 1 A–C, the final design of the 3D-printed µFFE is depicted. It is based on a single main 3D-printed part that includes as many required features as possible.

The main part includes the entire µFFE separation chamber, as well as the inlet and outlet chip-to-world connectors and interfaces, were 3D-printed in a single step. Additionally, two side parts, each containing an electrode chamber, holes for tubing, and a cavity for a contact tip, were also 3D-printed. The main part could be filled by four channels, of which the sample channel in the middle was flanked by two channels for buffer streams. An additional channel below was added to enable additional flushing, if necessary. Two slits at the sides of the separation chamber (with a height of 100 µm, width of 10 mm, and length of 29 mm) built the connection towards the cavity for the side parts. In between, commercially available polycarbonate membranes were placed. The purpose was to prevent bubbles from electrolysis to enter the main chamber. Novo et al. found for a PDMS-based device that a membrane pore size of 0.1 µm is optimal with regard to a low electrical resistance while an efficient removal of electrolysis-based bubbles can be ensured due to a high fluidic resistance/ trans-membrane resistance [7]. Moreover, by reliantly compartmentalizing the fluidics, balancing between the volume flows of the channels becomes unnecessary. From the main chamber, eight channels of the same length (with a height of 200 µm and a width of 700 µm) led towards 3D-printed wells for sample collection. Since the wells had the same distance to another as in a usual 96-well plate, multichannel pipettes could be used to transfer the collected sample fractions.

The entire µFFE setup was completed by the following steps: A 0.3 mm platinum wire was placed into the electrode chamber (with a height of 1.1 mm and a width of 0.5 mm) of the side part; a cut polycarbonate membrane was then inserted into the main part's cavity, where the side part was then inserted; and sealing was subsequently achieved by gluing. Importantly, this manufacturing process does not require chemical treatment of the membranes as presented by Novo et al.; instead, annealing was only applied to the sides, and the key parts separation chamber and outlet interface were built up in a single step via 3D printing. Finally, the contact tip and tubes for the electrode chambers were led through their holes in the side part—enabling a robust electrical connection between the platinum wire and the power supply, as well as purging bubbles in the electrode chambers, respectively.

In sum, this design enables an assembly-free setup of almost all of the device's main parts—that is, the inlets, outlets, and the separation chamber whose correct height is a critical parameter. Only the polycarbonate membranes and the platinum wires need to be separately incorporated. Furthermore, instead of chemical treatment, mechanical pressure applied through the side part is sufficient for creating leaking-free compartmentalization.

3.2 Printing resolution

Under the impact of an electric field, the main chamber height of any µFFE device is critical for band resolution and

the residence time of the sample [38]. Therefore, 3D printing resolution and chamber heights need to be known precisely and were determined by digital microscope measurements for µFFE devices with most relevant CAD heights of 100 and 200 µm, respectively (see Section 3.4 and 3.5). A 3D-printed structure with channel heights of 200 µm and its corresponding topographic picture is shown in Fig. 2A and C. The average channel height derived from a topographic profile (see Fig. 2B) was 91 ± 3 µm and 217 ± 4 µm for CAD heights of 100 µm and 200 µm, respectively. A systematic but reliable deviation of approx. -10% and $+10\%$ was measured for 100 and 200 µm CAD height, respectively. The surface roughness parameter "R_a" (an arithmetical mean deviation of the assessed profile) was determined as 8 µm. The average channel heights as a function of the number of outlets, the measurement position, and the technical replicate are shown in Fig. 2D, E, and F, respectively. Considering the standard deviations, identical heights were measured with regard to the channel, position or technical replicate. Therefore, a consistent 3D printing process can be assumed.

For some but not all parts, a slightly curved profile of the channels (see Fig. 2C) was observed. A probable cause could be the hot post-processing for wax removal. An impact on the stability might also have been the profile measurement on the open model (i.e., the final cover of the inner channels was removed and not printed). In the actual 3D printed µFFE devices, the top side is printed directly in one part, which causes a stabilization of the part (and the inner channel structures). It should be noted that the 3D printer prints in layers 32 µm thick [3], so there may be deviations from the actual printing process in this area. Since the actual height was independent of for example, channel number, there was no actual problem in terms of print reproducibility.

3.3 Chip-to-world interface

The collection and fractionation of samples is an important feature of microfluidic free-flow electrophoresis. The ability to transfer samples from the inside of a microfluidic chip to the sample collection and, if necessary, further processing is called "chip-to-world interface." Previous work focused on specific proof of concept experiments with low number of outlets of µFFE devices (e.g., two or three outlets) [11,25]. However, if fractionation and collection of samples is the main purpose (as is the case with the µFFE device presented in this paper), the number of outlets plays an important role, as it allows for determining the effective separation. In studies where a higher sample fractionation (e.g., with 9, 11 or 24 outlets) was obtained, this could only be achieved by using tubing connections or an elaborate assembly of a tubeless interface to the main device [25]. However, it is rather difficult to integrate tubing connections and alignment into microfluidic devices in such a way that reproducible outlet flow rates can be achieved [7]. To the best of our knowledge, we present the first directly integrated chip-to-world interface that does not rely on a manual alignment step or tubing.

Dividing a fluid stream into several outlets demands well-adjusted fractionation based on the hydrodynamic resistance of the outlet channels. The presented µFFE device enables fractionation into eight outlets with good precision, as gravimetrically investigated (see Fig. 3B). The relative standard deviation between different wells of all three technical replicates was 10.8% ($n = 3$), while the relative standard deviation of the first, second, and third replicate between different wells were comparable with 9.8, 12.3 and 9.9%, respectively. The highest average deviation from the ideal value was found in outlet #2 at -8%. Outlet #3 showed the lowest average standard deviation of all technical replicates at 5.5% and outlet #8 the highest at 23.8%. To provide a clearer overview, the wells are numerated and depicted in Fig. 3A.

The design allows any bubbles which might originate from degassing to predictably and readily flow upwards. Possibly, the outlet fractions might even regulate each other. Since they all are connected to each other, a change of volume height in one of the wells affects the others due to its pressure. Another detail of the design is the inter-well distance, which fits to multichannel pipettes.

A separation is only as good as its degree of fractionation, and future work might focus on further optimizing this basic design by incorporating more outlets. Nonetheless, the width of the separation channel could be a potential limiting factor. Due to its limited printing resolution in the *xy*-direction (data not shown), the number of outlet channels might be limited when all outlet channels should have the same hydrodynamic resistance [25].

3.4 Estimation of EOF

Based on the theoretical considerations of Dutta et al. [38], the impact of EOF can be estimated by the band broadening of a non-electrophoretically tracer compound (such as rhodamine B) under the influence of an electric field (see Fig. 4). Previously, Novo et al. [7] have applied this equation to estimate the electroosmotic mobility of a PDMS-based µFFE device. They reported similar results as Luo et al., who studied dynamic coating strategy to suppress electroosmosis in PDMS-based devices [36].

The apparent electroosmotic mobility μ_{EOF} is calculated as:

$$\mu_{EOF} = \sqrt{\frac{(\sigma_E^2 - \sigma_0^2)\, vD}{E^2 h^2 l}} \tag{1}$$

Band broadening is described as $\sigma_E^2 - \sigma_0^2$, where σ_E^2 is the band's variance under the impact of an electric field, and σ_0^2 is the band's variance at 0 V. D is the diffusion coefficient of rhodamine B (4.2×10^{-10} m²/s [41]); v is the hydrodynamic velocity (0.833 mm/s); E the strength of the electric field (97 V/cm); h the channel height (CAD depth of 200 µm); and l the length between sample inlet and point of measurement (29 mm).
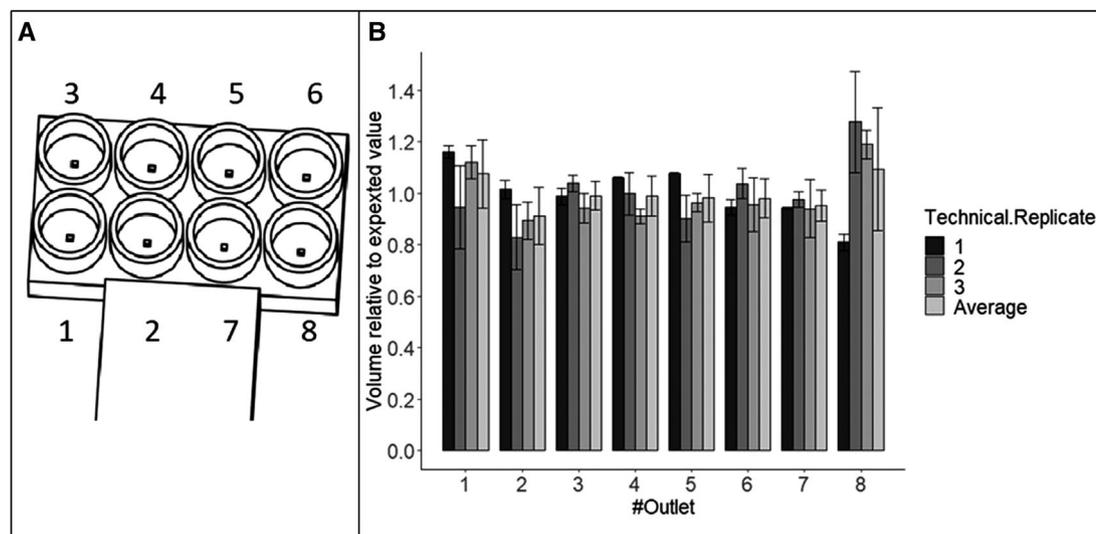
Figure 3. (A) CAD drawing of the wells (untransparent view). Numbering corresponds to the numbering of the outlet channels in Fig. 4. (B) Outlet flow fraction relative to the expected value of 1/8 for three technical replicated (error bars display the standard deviation for $n = 3$).
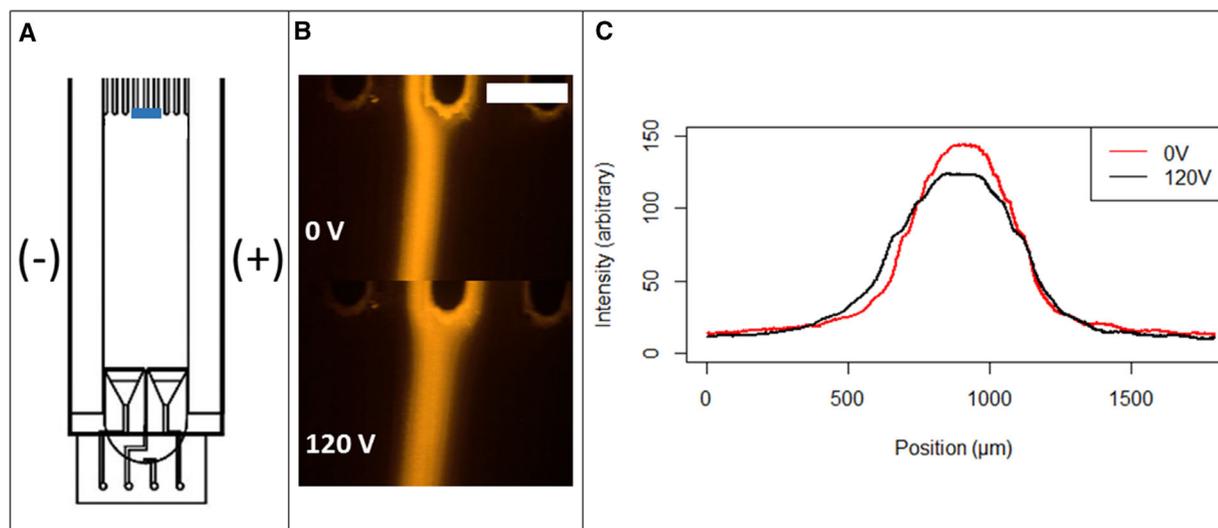
Figure 4. (A) CAD drawing of the main μFFE device. (−) and (+) indicate the polarity. The position of the measurement in picture B is depicted by a blue bar. (B) Fluorescence image of rhodamine B at different voltages. The white scale bar stands for 1 mm width. (C) Intensity profile of rhodamine B at different voltages.

Fitted to a Gaussian function by ImageJ [39,40], the band's standard deviation increased by 19 ± 25 μm ($n = 9$). According to Eq. (1), the apparent electroosmotic mobility (μ_{EOF}) of the 3D-printed μFFE device falls between $2.1 \times 10^{-10} \pm 2.5 \times 10^{-10}$ m²/Vs. Considering the measured channel height of 217 μm (see Section 3.2 for 3D printing resolution), the electroosmotic mobility might even be as low as $1.8 \times 10^{-10} \pm 2.2 \times 10^{-10}$ m²/Vs. Using the same buffer conditions and dynamic coating strategy based on 0.1% (w/w) HEC, Novo et al. estimated an apparent electroosmotic mobility of 3.2×10^{-8} m²/Vs [7]. The measured electroosmosis is therefore over 150–175 times smaller than in a PDMS-based device. Thus, electroosmosis was a negligible source of band broadening.

Although the exact composition is a corporate secret, based on the safety data sheet [42], the polyacrylic structure of the 3D printing material probably consists of a proportion of hydrophobic regions. It is therefore worth noting that electroosmosis might be suppressed at least in part due to a lack of surface charge [43].

3.5 Separation experiment

As a first proof of concept experiment, a mixture of three differently charged fluorescence dyes was applied to prove the functionality of the 3D-printed μFFE device, that is, rhodamine B (neutral charge) [44]; pyronin Y (monocation) [44];
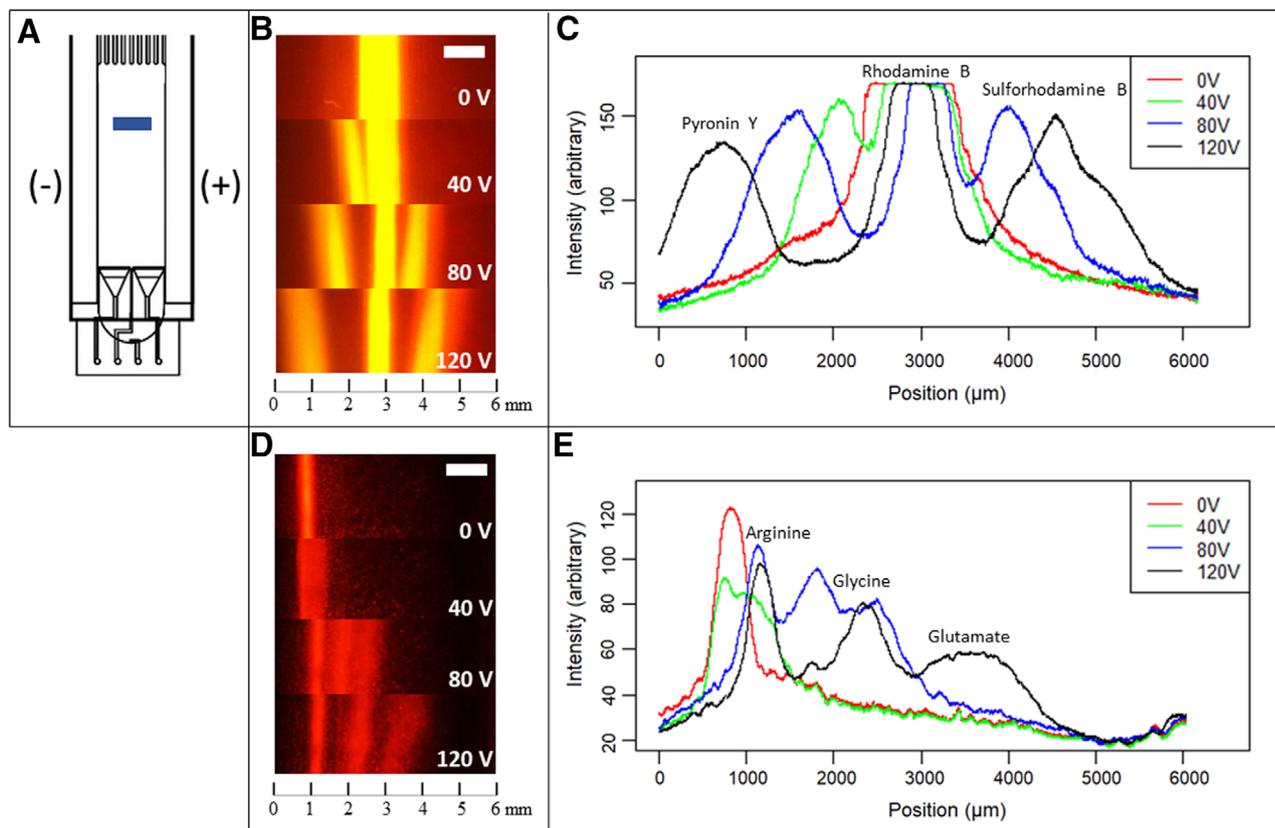
Figure 5. (A) CAD drawing of the main µFFE part. (−) and (+) indicate the polarity. The position of the fluorescence image in picture B is depicted by a blue line. (B) Fluorescence image of the separation of pyronin Y, rhodamine B, and sulforhodamine B at different voltages. The total volume flow rate of the separation buffer was set to 100 µL/min, the flow rate of the sample solution was set to 1 µL/min. The white scale bar stands for 1 mm width. (C) Intensity profile at different voltages over the width of picture B. (D) Fluorescence image of the separation of rhodamine B labeled glycine, glutamate, and arginine at different voltages. The total volume flow rate of the separation buffer was set to 200 µL/min, the flow rate of the sample solution was set to 2 µL/min. The white scale bar stands for 1 mm width. (E) Intensity profile at different voltages over the width of picture D.

and sulforhodamine B (monoanion) [45]. Fig. 5B shows the separation of these fluorescence dyes at different voltages. The pictures show the typical deflection at the mode of free-flow zone electrophoresis. Additionally, band broadening of pyronin Y and sulforhodamine B was observed (see Fig. 5B).

As shown in Fig. 5C, at sufficient high voltages (i.e., >80 V) all three fluorescence dyes could be characterized by distinct peaks. At a voltage of 120 V, the center of the very left peak (pyronin Y) and the center of the very right peak (sulforhodamine B) had a distance of 3.4 ± 0.6 mm (two technical replicates in triplicate). This clearly indicates a successful separation of the three fluorescence dyes which only differed by one to two charges per molecule.

To demonstrate the separation of biomolecules and separation of molecules with the same charge sign, the rhodamine B labeled amino acids arginine (neutral charge [46]), glycine (monoanion [46]), and glutamate (dianion [28,46]) were separated at different voltages (see Fig. 5D for the images and Fig. 5E for the profile). The left edge of the image represents the center of the main separation chamber. Especially two peaks moved towards the cathode. However, some motion of

the center of the far left peak (0.4 mm) was measured, possibly due to a slight flow variation. Distinguishable peaks were achieved above 80 V, while a voltage of 120 V enabled a separation of 1.1 mm from arginine (far left) to glycine (middle) and further 1.3 mm from glycine to glutamate (far right). The band broadening of glutamate in particular can be explained by the increase in electrophoretic motion due to additional charge. The deflection in a laminar flow profile is the cause of such an increase in variance and is well known for free-flow zone electrophoresis [38].

In summary, the separation of fluorescence dyes with different charge signs and amino acids with the same charge sign could be successfully demonstrated as proof of concept for the 3D-printed µFFE device by free-flow zone electrophoresis.

Few applications have been reported in the literature on the separation of two to four labeled amino acids [28,47–49], including the very first publication on microfluidic free-flow electrophoresis from Raymond et al. in 1994 [28]. One possible application is the separation of labeled biomolecules from unlabeled biomolecules and/or unbound labels (as

demonstrated in this work using amino acids and rhodamine B isothiocyanate as an example). However, a prerequisite for an electrophoretic separation is that the charge of the molecules be separated (here: labeled biomolecule and labeling agent) is different. Accordingly, all proteinogenic amino acids labeled with rhodamine B isothiocyanate (except arginine and lysine) can be purified separately.

4 Concluding remarks

This study presents a facilitated manufacturing strategy for an entire fully functional 3D-printed device for achieving microfluidic free-flow electrophoresis. As proof of concept, the separation of three fluorescence dyes as well as the separation of rhodamine B labeled amino acids (in both experiments the samples differ by one to two charges per molecule) by free-flow zone electrophoresis in the 3D-printed device was successfully demonstrated. The main μFFE parts—including the separation chamber and wells—are all 3D-printed in a single step. This approach supersedes potentially error-prone manual aligning steps that characterize more traditional PDMS-based designs or 3D printing that is based on fused deposition modeling (FDM). Moreover, this study presents integrated 3D-printed wells as a novel option for a chip-to-world interface and enabled a sample fractionation to eight outlets. Thus, the system shows great potential for applications where sample components are to be fractionated, for example, in downstream processing or sample pretreatment for further analysis. Especially for biotechnological processes continuous applications are of increasing interest. The miniaturized FFE device could be directly integrated into a cultivation process and thus enable a continuous separation of sample components, such as proteins or amino acids. Electrophoretic separation and subsequent fractionation would potentially reduce the sample complexity and thus facilitate the analysis of otherwise hardly distinguishable substances. The 3D-printed wells would serve as a flexible platform for sample transfer to an analytic method of choice. Future work could aim at a higher degree of fractionation (through a larger number of outlets), a disposable sample collection system, as well as the direct implementation of analytical devices.

The use of polycarbonate membranes as a compartmentalization strategy with a low electric resistance has been shown to be transferable to a design based on 3D printing technology. Moreover, the presented strategy does not require any chemical pretreatment of the membrane (as originally proposed). Instead, the membranes are simply placed into their appropriate cavity, and sealed by pressing and gluing the side part onto them—which substantially streamlines and simplifies the whole setup.

Notably and importantly, the biocompatibility of the material used in this study actually renders it a potential candidate for incorporation into a LoC system in for example, biological processes [13,14]. Future studies might seek to validate further modes of μFFE (e.g., isotachophoresis or isoelectric focusing) or to separate further biological samples, such as

proteins. Our study shows one major advantage of 3D printing due to the freedom of design and thus the possibility of directly integrating and connecting functional modules, for example, by direct incorporation of threaded fittings and interfaces [35,50]. Yet, the dimensions of the 3D-printed structures are limited by the printer resolution and are currently larger than those of PDMS microfluidics fabricated by soft lithography. Nevertheless, 3D printing technology is advancing rapidly, resolution is improving and printers with lower micron resolution are already available. Our work paves the way for a more flexible approach to the design and investigation of μFFE devices.

The authors have declared no conflict of interest.

5 References

[1] Waheed, S., Cabot, J. M., Macdonald, N. P., Lewis, T., Guijt, R. M., Paull, B., Breadmore, M. C., *Lab Chip* 2016, *16*, 1993–2013.

[2] Yazdi, A. A., Popma, A., Wong, W., Nguyen, T., Pan, Y. Y., Xu, J., *Microfluid. Nanofluid.* 2016, *20*, 18.

[3] Enders, A., Siller, I. G., Urmann, K., Hoffmann, M. R., Bahnemann, J., *Small* 2019, *15*, 9.

[4] Bhattacharjee, N., Urrios, A., Kanga, S., Folch, A., *Lab Chip* 2016, *16*, 1720–1742.

[5] Siller, I. G., Preuss, J. A., Urmann, K., Hoffmann, M. R., Scheper, T., Bahnemann, J., *Sensors* 2020, *20*, 16.

[6] Saar, K. L., Peter, Q., Muller, T., Challa, P. K., Herling, T. W., Knowles, T. P. J., *Microsyst. Nanoeng.* 2019, *5*, 10.

[7] Novo, P., Dell'Aica, M., Jender, M., Hoving, S., Zahedi, R. P., Janasek, D., *Analyst* 2017, *142*, 4228–4239.

[8] Duffy, D. C., McDonald, J. C., Schueller, O. J. A., Whitesides, G. M., *Anal. Chem.* 1998, *70*, 4974–4984.

[9] Gabriel, E. F. M., Coltro, W. K. T., Garcia, C. D., *Electrophoresis* 2014, *35*, 2325–2332.

[10] Guckenberger, D. J., de Groot, T. E., Wan, A. M. D., Beebe, D. J., Young, E. W. K., *Lab Chip* 2015, *15*, 2364–2378.

[11] Anciaux, S. K., Geiger, M., Bowser, M. T., *Anal. Chem.* 2016, *88*, 7675–7682.

[12] Anciaux, S. K., Bowser, M. T., *Electrophoresis* 2020, *41*, 225–234.

[13] Siller, I. G., Enders, A., Gellermann, P., Winkler, S., Lavrentieva, A., Scheper, T., Bahnemann, J., *Biomed. Mater.* 2020, *15*, 055007.

[14] Siller, I. G., Enders, A., Steinwedel, T., Epping, N. M., Kirsch, M., Lavrentieva, A., Scheper, T., Bahnemann, J., *Materials* 2019, *12*, 17.

[15] Jing, M., Bowser, M. T., *Lab Chip* 2011, *11*, 3703–3709.

[16] Persat, A., Marshall, L. A., Santiago, J. G., *Anal. Chem.* 2009, *81*, 9507–9511.

[17] Novo, P., Jender, M., Dell'Aica, M., Zahedi, R. P., Janasek, D., I. Barsony, Z. Zolnai, G. Battistig (Eds.),in: *Proceedings of the 30th Anniversary Eurosensors Conference - Eurosensors 2016*, Elsevier Science Bv, Amsterdam 2016, p. 1382–1385.

[18] Walowski, B., Huttner, W., Wackerbarth, H., *Anal. Bioanal. Chem.* 2011, *401*, 2465–2471.

[19] Wang, P. L., Zhang, L. H., Shan, Y. C., Cong, Y. Z., Liang, Y., Han, B., Liang, Z., Zhang, Y. K., *J. Sep. Sci.* 2010, *33*, 2039–2044.

[20] Wen, J., Wilker, E. W., Yaffe, M. B., Jensen, K. F., *Anal. Chem.* 2010, *82*, 1253–1260.

[21] Nagl, S., *Eng. Life Sci.* 2018, *18*, 114–123.

[22] Podszun, S., Vulto, P., Heinz, H., Hakenberg, S., Hermann, C., Hankemeier, T., Urban, G. A., *Lab Chip* 2012, *12*, 451–457.

[23] Puchberger-Enengl, D., Podszun, S., Heinz, H., Hermann, C., Vulto, P., Urban, G. A., *Biomicrofluidics* 2011, *5*, 10.

[24] Kohlheyer, D., Eijkel, J. C. T., van den Berg, A., Schasfoort, R. B. M., *Electrophoresis* 2008, *29*, 977–993.

[25] Novo, P., Janasek, D., *Anal. Chim. Acta* 2017, *991*, 9–29.

[26] Fonslow, B. R., Barocas, V. H., Bowser, M. T., *Anal. Chem.* 2006, *78*, 5369–5374.

[27] Xu, Y., Zhang, C. X., Janasek, D., Manz, A., *Lab Chip* 2003, *3*, 224–227.

[28] Raymond, D. E., Manz, A., Widmer, H. M., *Anal. Chem.* 1994, *66*, 2858–2865.

[29] Albrecht, J. W., Jensen, K. F., *Electrophoresis* 2006, *27*, 4960–4969.

[30] Wen, J. A., Albrecht, J. W., Jensen, K. F., *Electrophoresis* 2010, *31*, 1606–1614.

[31] Fu, X. T., Mavrogiannis, N., Ibo, M., Crivellari, F., Gagnon, Z. R., *Electrophoresis* 2017, *38*, 327–334.

[32] Janasek, D., Schilling, M., Manz, A., Franzke, J., *Lab Chip* 2006, *6*, 710–713.

[33] Kohlheyer, D., Eijkel, J. C. T., Schlautmann, S., van den Berg, A., Schasfoort, R. B. M., *Anal. Chem.* 2008, *80*, 4111–4118.

[34] Herzog, C., Jochem, G. F. W., Glaeser, P., Nagl, S., *Microchim. Acta* 2015, *182*, 887–892.

[35] Barbaresco, F., Cocuzza, M., Pirri, C. F., Marasso, S. L., *Nanomaterials* 2020, *10*, 14.

[36] Luo, Y. Q., Huang, B., Wu, H., Zare, R. N., *Anal. Chem.* 2006, *78*, 4588–4592.

[37] 3d Systems Inc., *EasyClean Post Processing Guide for All MJP Materials*, http://infocenter.3dsystems.com/mjplibrary/mjp-easyclean-hardware-setup-settings-guide/easyclean-post-processing-guide-all-mjp-materials, last accessed September 2020.

[38] Dutta, D., *J. Chromatogr. A* 2015, *1404*, 124–130.

[39] Schindelin, J., Arganda-Carreras, I., Frise, E., Kaynig, V., Longair, M., Pietzsch, T., Preibisch, S., Rueden, C., Saalfeld, S., Schmid, B., Tinevez, J. Y., White, D. J., Hartenstein, V., Eliceiri, K., Tomancak, P., Cardona, A., *Nat. Methods* 2012, *9*, 676–682.

[40] Rueden, C. T., Schindelin, J., Hiner, M. C., DeZonia, B. E., Walter, A. E., Arena, E. T., Eliceiri, K. W., *BMC Bioinformatics* 2017, *18*, 26.

[41] Gendron, P. O., Avaltroni, F., Wilkinson, K. J., *J. Fluoresc.* 2008, *18*, 1093–1101.

[42] 3d Systems Inc., *VisiJet M2R-CL (MJP)*, https://de.3dsystems.com/materials/visijet-m2r-cl-mjp, last accessed April 2020.

[43] Ghosal, S., *Electrophoresis* 2004, *25*, 214–228.

[44] Mai, M. S., Allison, W. S., *Arch. Biochem. Biophys.* 1983, *221*, 467–476.

[45] Corrie, J. E. T., Eccleston, J. F., Ferenczi, M. A., Moore, M. H., Turkenburg, J. P., Trentham, D. R., *J. Phys. Org. Chem.* 2008, *21*, 286–298.

[46] Minihan, S., *Biochem. Educ.* 1983, *11*, 41–42.

[47] Jezierski, S., Gitlin, L., Nagl, S., Belder, D., *Anal. Bioanal. Chem.* 2011, *401*, 2651–2656.

[48] Jezierski, S., Tehsmer, V., Nagl, S., Belder, D., *Chem. Commun.* 2013, *49*, 11644–11646.

[49] Zhou, W. J., Xia, L., Xiao, X. H., Li, G. K., Pu, Q. S., *Electrophoresis* 2019, *40*, 2165–2171.

[50] Chen, C. P., Mehl, B. T., Munshi, A. S., Townsend, A. D., Spence, D. M., Martin, R. S., *Anal. Methods* 2016, *8*, 6005–6012.